Statistically optimal estimation of surface mass anomalies by directly using GRACE level-2 spherical harmonic coefficients as measurements

Chang, Guobin ; Qian, Nijia; Bian, Shaofeng

DOI
10.1093/gji/ggad024

Publication date
2023

Document Version
Final published version

Published in
Geophysical Journal International

Citation (APA)
Chang, G., Qian, N., & Bian, S. (2023). Statistically optimal estimation of surface mass anomalies by directly using GRACE level-2 spherical harmonic coefficients as measurements. *Geophysical Journal International*, *233*(3), 1786–1799. https://doi.org/10.1093/gji/ggad024

Geophysical Journal International

Geophys. J. Int. (2023) **233,** 1786–1799
Advance Access publication 2023 January 23
GJI Gravity, Geodesy and Tides

https://doi.org/10.1093/gji/ggad024

Statistically optimal estimation of surface mass anomalies by directly using GRACE level-2 spherical harmonic coefficients as measurements

Guobin Chang [1,2] Nijia Qian[3,4] and Shaofeng Bian[1]

[1] *School of Geography and Information Engineering, China University of Geosciences (Wuhan), Wuhan* 430074, *China. E-mail: guobinchang@hotmail.com*
[2] *State Key Laboratory of Geo-Information Engineering, Xi'an Research Institute of Surveying and Mapping, Xi'an* 710054, *China*
[3] *School of Environment Science and Spatial Informatics, China University of Mining and Technology, Xuzhou* 221116, *China*
[4] *Department of Geoscience and Remote Sensing, Delft University of Technology, CN Delft* 2628, The Netherlands

Accepted 2023 January 4. Received 2023 January 4; in original form 2022 May 23

SUMMARY

Point-mass inversion is widely employed in GRACE level-2 data processing. Conventionally, the spherical harmonic (SH) coefficients are used indirectly: a set of pseudo measurements is generated first using the SH coefficients through SH synthesis; then the point-mass inversion is done with these pseudo measurements. To be statistically optimal, the covariance matrix of pseudo measurements should be calculated and used to appropriately weigh the parameter estimation. In this work, we propose a statistically optimal point-mass inversion scheme by directly using the SH coefficients as measurements. We prove the equivalence between this direct approach and the conventional indirect approaches. We also demonstrated their comparable performance through both simulation and real GRACE data processing. Choosing and calculating pseudo measurements, propagating covariance matrix and potentially dealing with the singularity of the covariance matrix involved in the conventional indirect approaches are avoided in the proposed direct approach. This statistically optimal direct approach can readily be employed in mascon inversion of GRACE data and other radial basis functions-based approaches in regional gravity modeling.

Key words: Global change from geodesy; GRACE; Mass anomaly; Satellite gravity; Time variable gravity.

1 INTRODUCTION

Mass redistributions inferred from GRACE data find wide applications in geoscientific studies (Tapley *et al.* 2019). For calculating surface mass anomalies from GRACE level-2 products, i.e. the spherical harmonic (SH) or Stokes coefficients, there can be three different approaches. The first is a conversion, in which a simple SH synthesis can directly produce surface mass anomalies (Wahr *et al.* 1998). However, this approach requires preprocessed filtering or smoothing, leading to decreased spatial resolution and signal leakage of mass anomalies. The second and the third are point-mass inversion (Baur & Sneeuw 2011) and mascon inversion (Schrama & Wouters 2011), respectively. In the point-mass approach, the surface mass anomalies are assumed to be concentrated on some discrete points; while in the mascon approach, they are uniformly distributed within different surface patches. Both point-mass and mascon approaches can produce well-localized and high-resolution estimates and do not need any filtering and smoothing, though their calculations are more complex than SH conversion (Wouters *et al.* 2014). In this study, we mainly focus on point-mass inversion, with a brief discussion on the mascon inversion.

In recent years, point-mass inversion found wide applications, (see e.g. Baur & Sneeuw 2011; Barletta *et al.* 2013; Forsberg *et al.* 2017; Sørensen *et al.* 2017; Richter *et al.* 2019; Su *et al.* 2019; Ferreira *et al.* 2020a,b). This inversion links the pseudo measurements (calculated using SH coefficients) situated at GRACE-orbit height to the point-mass on the Earth surface. There are many choices for pseudo measurements, such as potential, geoid height, gravity anomaly and gravity disturbances and the number and the distribution of pseudo measurements are not unique either. With synthesized pseudo measurements, one can do a weighted least-squares estimation with the help of their covariance matrix, which is propagated from the covariance information of the original SH coefficients. This is statistically optimal and promoted recently in Ran *et al.* (2018a,b). Note that statistically optimal treatment of the pseudo measurements is proposed for mascons in Ran *et al.* (2018a,b); however, it can be readily applicable in a point-mass inversion. To summarize, when using the conventional inversion

approaches, one needs to choose which type of pseudo measurements is to use, determine how many pseudo measurements are to generate, define how they are distributed and finally deal with the (potential) singularity of the covariance matrix of pseudo measurements.

In this study, we propose to directly use the SH coefficients as measurements, without making the above choices and calculating pseudo measurements. It will be proven that the same statistical optimality can also be achieved: we need only weigh the measurements (SH coefficients) with the inverse of the corresponding covariance matrix. Thereby, covariance matrix propagation and dealing with the potential singularity of the propagated covariance matrix involved in conventional inversion approaches will be avoided. We will also prove and demonstrate the validity of the proposed approach and its equivalence to the conventional approaches theoretically and experimentally. For easy citing, we call the proposed approach the 'Direct Approach' (DA) and the conventional ones 'Indirect Approaches' (IAs) in the following.

This paper is organized as follows: in Section 2, the methodology is detailed, including the introduction of DA and IA, the proof of their equivalence and a brief extension for the case of mascon. Numerical experiments are presented in Section 3, including both simulation and real GRACE data processing. The conclusions are followed in Section 4.

2 THEORETICAL PROOF

In this section, the measurement models for a statistically optimal IA and the DA are presented in Sections 2.1 and 2.2, respectively. A theoretical proof of the equivalence between the IA and the DA is given in Section 2.3. The mascon case is briefly discussed in Section 2.4.

2.1 Indirect approach

The computations for IA inversion can be split into the following two steps. First, a set of pseudo measurements at satellite altitude, taking anomalous gravity potentials as an example, is generated using GRACE level-2 products. The *i*-th pseudo measurements T reads as follows:

$$T(\boldsymbol{x}_i) = \frac{Gm_0}{R}\sum_{l=1}^{M}\left(\frac{R}{|\boldsymbol{x}_i|}\right)^{l+1}\sum_{m=-l}^{l} c_{\mathrm{lm}}Y_{\mathrm{lm}}(\tilde{\boldsymbol{x}}_i) \tag{1}$$

where Gm_0 denotes the geocentric constant; R denotes the semi-major axis of the reference ellipsoid; M denotes the maximum degree; $\boldsymbol{x}$ denotes the coordinate vector of the point at which gravity potential is to be evaluated; C_{lm} represents the monthly SH coefficients with the long-term mean or trend removed; Y_{lm} denotes the fully normalized spherical harmonics. A vector with a tilde over denotes its corresponding normalized vector.

The second step is to link the produced pseudo measurements at satellite altitude to point-masses on the Earth's surface. This is based on the point-mass radial basis representation of the anomalous gravity potential, expressed as follows:

$$T(\boldsymbol{x}) = G\sum_{j=1}^{N}\beta_j\Psi(\boldsymbol{x},\boldsymbol{z}_j) + \varepsilon \tag{2}$$

with,

$$\Psi(\boldsymbol{x},\boldsymbol{z}) = \frac{1}{|\boldsymbol{x}-\boldsymbol{z}|} = \sum_{l=1}^{M}\frac{R^l}{(2l+1)|\boldsymbol{x}|^{l+1}}\sum_{m=-l}^{l}Y_{\mathrm{lm}}(\tilde{\boldsymbol{x}})\,Y_{\mathrm{lm}}(\tilde{\boldsymbol{z}}) \tag{3}$$

In eq. (2), the coordinate vector of the *j*-th point-mass is denoted as $\boldsymbol{z}_j$; there are totally N such point-masses in the above model; the point-mass β_j is to be estimated; ε is the measurement noise. Combining eqs (1)–(3) results in the functional model which relates the pseudo measurements at satellite altitude to the point-masses on the Earth's surface. Stacking all the pseudo measurements as $\mathbf{z} = [\,T(\mathbf{x}_1)\;T(\mathbf{x}_2)\cdots T(\mathbf{x}_K)\,]^{\mathrm{T}}$ and all the point-masses as $\beta = [\,\beta_1\;\beta_2\cdots\beta_N\,]^{\mathrm{T}}$, the measurement model of IA inversion in vector-matrix form is as follows:

$$\boldsymbol{z} = \boldsymbol{B}\boldsymbol{\beta} + \boldsymbol{\varepsilon} \tag{4}$$

where $\boldsymbol{B} = G\begin{bmatrix}\Psi(\boldsymbol{x}_1,\boldsymbol{z}_1) & \cdots & \Psi(\boldsymbol{x}_1,\boldsymbol{z}_N)\\ \vdots & \ddots & \vdots \\ \Psi(\boldsymbol{x}_K,\boldsymbol{z}_1) & \cdots & \Psi(\boldsymbol{x}_K,\boldsymbol{z}_N)\end{bmatrix}$ denotes design matrix; $\boldsymbol{\varepsilon}$ represents measurement error vector. In this study, we assume that there is only measurement error and no modeling error in $\boldsymbol{\varepsilon}$. Finally, the statistically optimal estimate of the surface mass anomaly is defined as follows:

$$\hat{\beta} = \arg\min_{\beta} f(\beta) = \arg\min_{\beta}\left[(\mathbf{z}-\mathbf{B}\beta)^{\mathrm{T}}\mathbf{P}^{-1}(\mathbf{z}-\mathbf{B}\beta) + g(\beta)\right] \tag{5}$$

where g($\boldsymbol{\beta}$) denotes the other part of the cost function which may correspond to some constraints on $\boldsymbol{\beta}$ in a regularization inversion. For regional gravity modeling, g($\boldsymbol{\beta}$) can also include the cost function concerning the fitting of other terrestrial data (Klees *et al.* 2018, 2019;

Slobbe *et al.* 2019). Let $\boldsymbol{F} = \frac{Gm_0}{R}\begin{bmatrix} \left(\frac{R}{|\boldsymbol{x}_1|}\right)^1 Y_{00}(\tilde{\boldsymbol{x}}_1) & \cdots & \left(\frac{R}{|\boldsymbol{x}_1|}\right)^{M+1} Y_{MM}(\tilde{\boldsymbol{x}}_1) \\ \vdots & \ddots & \vdots \\ \left(\frac{R}{|\boldsymbol{x}_K|}\right)^1 Y_{00}(\tilde{\boldsymbol{x}}_K) & \cdots & \left(\frac{R}{|\boldsymbol{x}_K|}\right)^{M+1} Y_{MM}(\tilde{\boldsymbol{x}}_K) \end{bmatrix}$. Let $\boldsymbol{y}$ denote the vector of SH coefficients c_{lm}. From eq. (1), we have

$$\begin{cases} \boldsymbol{z} = \boldsymbol{F}\boldsymbol{y} \\ \boldsymbol{\varepsilon} = \boldsymbol{F}\boldsymbol{e} \end{cases} \tag{6}$$

where $\boldsymbol{e}$ denotes the measurement error vector of $\boldsymbol{y}$, assumed to be Gaussian distributed. So, $\boldsymbol{P} = \mathrm{cov}[\boldsymbol{\varepsilon}] = \boldsymbol{F}\mathrm{cov}[\boldsymbol{e}]\boldsymbol{F}^{\mathrm{T}} = \boldsymbol{F}\boldsymbol{Q}\boldsymbol{F}^{\mathrm{T}}$, where $\boldsymbol{Q}$ is the variance-covariance matrix of GRACE monthly solutions. This shows the clear linear relation between the pseudo measurement vector $\boldsymbol{z}$ and the original measurement vector $\boldsymbol{y}$ and this linear relationship will be vital for our proof.

2.2 Direct approach

In the DA, we directly treat SH coefficients as measurements. By comparing eq. (1) with eq. (2) and eq. (3), we can obtain the following relationship between SH coefficients and point-masses (Schmidt *et al.* 2007; Wittwer 2009):

$$c_{lm} = \frac{1}{(2l+1)\,m_0} \sum_{j=1}^{N} \beta_j Y_{lm}\left(\tilde{\mathbf{z}}_j\right) + e \tag{7}$$

where e is the measurement noise. Then based on eq. (7), we have the following measurement equation in vector-matrix form:

$$\boldsymbol{y} = \boldsymbol{A}\boldsymbol{\beta} + \boldsymbol{e} \tag{8}$$

with,

$$\boldsymbol{A} = \frac{1}{m_0}\begin{bmatrix} Y_{00}\left(\tilde{\mathbf{z}}_1\right) & \cdots & Y_{00}\left(\tilde{\mathbf{z}}_N\right) \\ \vdots & \ddots & \vdots \\ \frac{1}{2M+1} Y_{MM}\left(\tilde{\mathbf{z}}_1\right) & \cdots & \frac{1}{2M+1} Y_{MM}\left(\tilde{\mathbf{z}}_N\right) \end{bmatrix} \tag{9}$$

Note that eq. (8) is exactly the measurement model of the proposed DA inversion. The optimal estimate with this measurement model is accordingly defined as follows:

$$\hat{\beta} = \arg\min_{\beta} h\left(\beta\right) = \arg\min_{\beta} \left[\left(\mathbf{y} - \mathbf{A}\beta\right)^{\mathrm{T}} \mathbf{Q}^{-1} \left(\mathbf{y} - \mathbf{A}\beta\right) + g\left(\beta\right)\right] \tag{10}$$

The term $g(\boldsymbol{\beta})$ in eq. (10) should be the same as that in eq. (5). This means that in the DA and IA, we are using the same terrestrial data set or the same regularization (including both regularization matrix and regularization parameter). By doing this, we can make a fair comparison between the two approaches: the differences between the two approaches, if any, are solely caused by different representation of the gravity measurements, i.e. $\boldsymbol{z}$ in eq. (4) vs. $\boldsymbol{y}$ in eq. (8).

2.3 A theoretical proof of the equivalence between the indirect and the direct approaches

In eq. (6), it is possible to find a set of locations, which make the matrix $\boldsymbol{F}$ square and invertible. In order for $\boldsymbol{F}$ to be invertible in a numerically stable manner, the locations should be globally distributed, rather than being confined to the target area and its buffer zone. Combining eq. (6) with eq. (8), we get the following relation:

$$\boldsymbol{z} = \boldsymbol{F}\boldsymbol{y} = \boldsymbol{F}\boldsymbol{A}\boldsymbol{\beta} + \boldsymbol{F}\boldsymbol{e} = \boldsymbol{F}\boldsymbol{A}\boldsymbol{\beta} + \boldsymbol{\varepsilon} \tag{11}$$

The invertibility of $\boldsymbol{F}$ implies that the information in $\boldsymbol{y}$ is ideally coded in $\boldsymbol{z}$ without any information loss. Pseudo measurements other than those in $\boldsymbol{z}$ are unnecessary because of this ideal coding. Any variable other than those in $\boldsymbol{z}$ must be a linear combination of $\boldsymbol{z}$. Augmenting this variable into $\boldsymbol{z}$ adds no new information in terms of estimating $\boldsymbol{\beta}$; and this may further cause the singularity of the covariance matrix. Following Schmidt *et al.* (2007), $\boldsymbol{z}$ with such an invertible matrix $\boldsymbol{F}$ can be called an admissible representation of $\boldsymbol{y}$.

Let $\boldsymbol{f}_i^{\mathrm{T}}$ denote the i-th row of $\boldsymbol{F}$. Let $\boldsymbol{a}_j$ denote the j-th column of $\boldsymbol{A}$. From eq. (1) and eq. (9), the element of the i-th row and j-th column in $\boldsymbol{FA}$ is expressed as follows:

$$\begin{aligned}
\{\mathbf{FA}\}_{ij} &= \mathbf{f}_i^{\mathrm{T}}\mathbf{a}_j \\
&= \left(\frac{Gm_0}{R}\left[\begin{array}{ccc} \frac{R}{|\mathbf{x}_i|}Y_{00}\left(\tilde{\mathbf{x}}_i\right) & \cdots & \left(\frac{R}{|\mathbf{x}_i|}\right)^{M+1}Y_{MM}\left(\tilde{\mathbf{x}}_i\right)\end{array}\right]\right)\left(\frac{1}{m_0}\left[\begin{array}{c} Y_{00}\left(\tilde{\boldsymbol{z}}_N\right) \\ \vdots \\ \frac{1}{2M+1}Y_{MM}\left(\tilde{\boldsymbol{z}}_N\right)\end{array}\right]\right) \\
&= G\sum_{l=0}^{M}\frac{R^l}{(2l+1)\left|\mathbf{x}_i\right|^{l+1}}\sum_{m=-l}^{l}Y_{lm}\left(\tilde{\mathbf{x}}_i\right)Y_{lm}\left(\tilde{\boldsymbol{z}}_j\right) \\
&= G\Psi\left(\boldsymbol{x}_i,\boldsymbol{z}_j\right) \\
&= \{\mathbf{B}\}_{ij}
\end{aligned} \tag{12}$$

which is equivalent to the following in matrix form:

$$\boldsymbol{B} = \boldsymbol{FA} \tag{13}$$

which clearly shows the relation between the design matrix of IA and that of DA. This relation is vital for our theoretical proof and will also be validated experimentally in the following numerical studies.

With an invertible $\boldsymbol{F}$ and according to eq. (13), we have the following:

$$\begin{aligned}
f(\beta) &= (\mathbf{z}-\mathbf{B}\beta)^{\mathrm{T}}\mathbf{P}^{-1}(\mathbf{z}-\mathbf{B}\beta)+g(\beta) \\
&= (\mathbf{Fy}-\mathbf{FA}\beta)^{\mathrm{T}}\left(\mathbf{FQF}^{\mathrm{T}}\right)^{-1}(\mathbf{Fy}-\mathbf{FA}\beta)+g(\beta) \\
&= (\mathbf{y}-\mathbf{A}\beta)^{\mathrm{T}}\mathbf{F}^{\mathrm{T}}\left(\mathbf{FQF}^{\mathrm{T}}\right)^{-1}\mathbf{F}(\mathbf{y}-\mathbf{A}\beta)+g(\beta) \\
&= (\mathbf{y}-\mathbf{A}\beta)^{\mathrm{T}}\mathbf{F}^{\mathrm{T}}\mathbf{F}^{-\mathrm{T}}\mathbf{Q}^{-1}\mathbf{F}^{-1}\mathbf{F}(\mathbf{y}-\mathbf{A}\beta)+g(\beta) \\
&= (\mathbf{y}-\mathbf{A}\beta)^{\mathrm{T}}\mathbf{Q}^{-1}(\mathbf{y}-\mathbf{A}\beta)+g(\beta) \\
&= h(\beta)
\end{aligned} \tag{14}$$

This means that the cost function of the IA inversion in eq. (5) exactly equals to that of the DA inversion in eq. (10). So the point-mass estimate defined in eq. (5) should be equal to that in eq. (10). This proves the equivalence between IA and DA. So with DA, we can directly treat the SH coefficients as measurements for estimating point-masses in the same statistically optimal way as that in a statistically optimal IA. In the DA, we do not need to choose or generate any pseudo measurements; and consequently, we do not either need to do covariance propagation or (potentially) deal with the involved singularity.

2.4 Proof for the mascon case

For mascon inversion, the measurement model of IA can be the same form as in eq. (4), however with the design matrix defined as follows:

$$\boldsymbol{B} = G\left[\begin{array}{ccc} \int_{\Omega_1}\Psi\left(\boldsymbol{x}_1,\boldsymbol{z}\right)\mathrm{d}\sigma_z & \cdots & \int_{\Omega_N}\Psi\left(\boldsymbol{x}_1,\boldsymbol{z}\right)\mathrm{d}\sigma_z \\ \vdots & \ddots & \vdots \\ \int_{\Omega_1}\Psi\left(\boldsymbol{x}_K,\boldsymbol{z}\right)\mathrm{d}\sigma_z & \cdots & \int_{\Omega_N}\Psi\left(\boldsymbol{x}_K,\boldsymbol{z}\right)\mathrm{d}\sigma_z\end{array}\right] \tag{15}$$

In the above, Ω_j denotes the region of the j-th mascon and $\mathrm{d}\sigma_z$ denotes the surface area elements corresponding to the argument $\boldsymbol{z}$. Similarly, the measurement model of DA has the same form as in eq. (8), but with the design matrix defined as follows:

$$\boldsymbol{A} = \frac{1}{m_0}\left[\begin{array}{ccc} \int_{\Omega_1}Y_{00}\left(\tilde{\boldsymbol{z}}_1\right)\mathrm{d}\sigma_z & \cdots & \int_{\Omega_N}Y_{00}\left(\tilde{\boldsymbol{z}}_N\right)\mathrm{d}\sigma_z \\ \vdots & \ddots & \vdots \\ \frac{1}{2M+1}\int_{\Omega_1}Y_{MM}\left(\tilde{\boldsymbol{z}}_1\right)\mathrm{d}\sigma_z & \cdots & \frac{1}{2M+1}\int_{\Omega_N}Y_{MM}\left(\tilde{\boldsymbol{z}}_N\right)\mathrm{d}\sigma_z\end{array}\right] \tag{16}$$

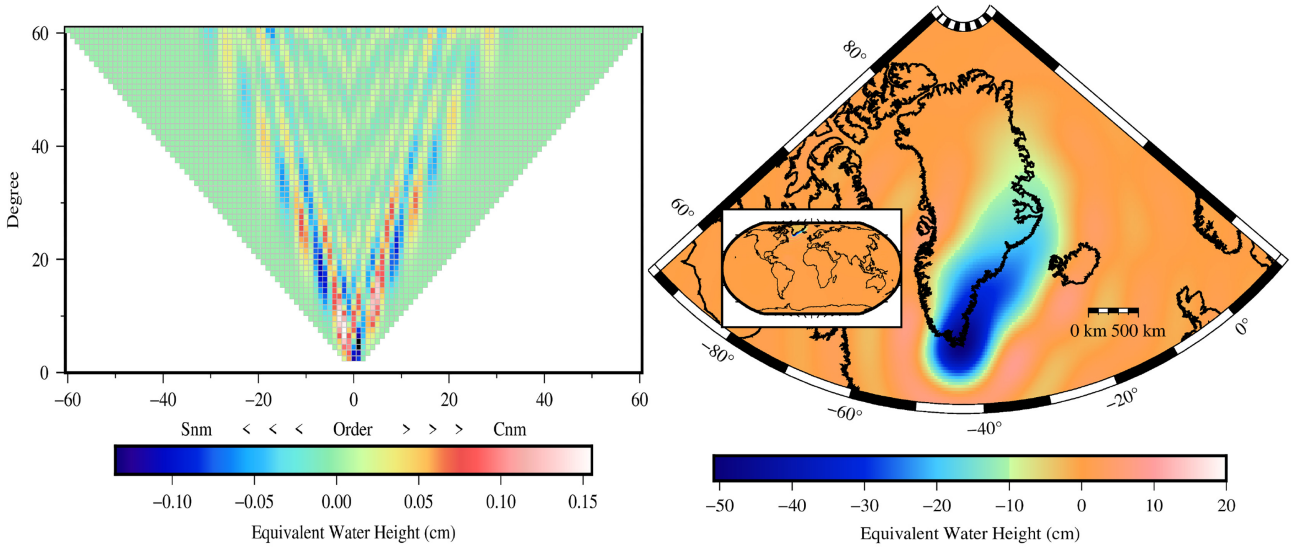

Figure 1. The simulated truths of mass anomaly signals in southeast Greenland in both spectral (a) and spatial (b) domains. Degree-0 and degree-1 terms are not considered here.

Then eq. (12) can be modified accordingly for the mascon case as follows:

$$
\begin{aligned}
\{\mathbf{FA}\}_{ij} &= \mathbf{f}_i^{\mathrm{T}}\mathbf{a}_j \\
&= \left(\frac{Gm_0}{R}\left[\frac{R}{|\mathbf{x}_i|}Y_{00}\left(\tilde{\mathbf{x}}_i\right)\cdots\left(\frac{R}{|\mathbf{x}_i|}\right)^{M+1}Y_{MM}\left(\tilde{\mathbf{x}}_i\right)\right]\right)\left(\frac{1}{m_0}\begin{bmatrix}\int_{\Omega_N}Y_{00}\left(\tilde{\boldsymbol{z}}_N\right)\mathrm{d}\sigma_z\\ \vdots \\ \frac{1}{2M+1}\int_{\Omega_N}Y_{MM}\left(\tilde{\boldsymbol{z}}_N\right)\mathrm{d}\sigma_z\end{bmatrix}\right) \\
&= G\sum_{l=0}^{M}\frac{R^l}{(2l+1)\left|\mathbf{x}_i\right|^{l+1}}\sum_{m=-l}^{l}Y_{lm}\left(\tilde{\mathbf{x}}_i\right)\int_{\Omega_N}Y_{lm}\left(\tilde{\boldsymbol{z}}_j\right)\mathrm{d}\sigma_z \\
&= G\int_{\Omega_N}\left[\sum_{l=0}^{M}\frac{R^l}{(2l+1)\left|\mathbf{x}_i\right|^{l+1}}\sum_{m=-l}^{l}Y_{lm}\left(\tilde{\mathbf{x}}_i\right)Y_{lm}\left(\tilde{\boldsymbol{z}}_j\right)\right]\mathrm{d}\sigma_z \\
&= G\int_{\Omega_N}\Psi\left(\boldsymbol{x}_i,\boldsymbol{z}_j\right)\mathrm{d}\sigma_z \\
&= \{\mathbf{B}\}_{ij}
\end{aligned}
\tag{17}
$$

For the mascon case, the same equation as in eq. (13) also holds. Finally, the same proof as in Section 2.3 holds for the mascon case.

Note that eq. (16) is exactly the design matrix of mascon inversion using GRACE level-2 data proposed in Jacob *et al.* (2012) and also the right factor matrix of the design matrix in the mascon inversion using GRACE level-1b data, e.g. the $\boldsymbol{L}$ matrix in Croteau *et al.* (2020). The design matrix of the IA in eq. (15) is exactly the design matrix of the so-called space-domain inversion approach proposed in Yi & Sun (2014), in which the approach proposed in Jacob *et al.* (2012) is called a spectral-domain inversion approach. The DA and IA for the mascon case, discussed in above, can be viewed as the statistically optimal version of the spectral- and spatial-domain inversions, respectively. Although the statistically optimal versions are equivalent to each other as proved in the above, this does not necessarily apply to their original versions, even when they do the same preprocessing of the SH coefficients before estimating the mascon parameters; because in general, independent and identically distributed (iid) errors in the spectral domain will not result in iid errors in the spatial domain and vice versa (Klees *et al.* 2008).

As a final note, the spectral consistency issue considered in Ran *et al.* (2018b), that is, appropriately truncating the series of eq. (3), is irrelevant in the DA. Or in other words, the DA is automatically spectrally consistent.

3 NUMERICAL STUDY

We conduct both closed-loop simulation and real GRACE data analysis of IA and DA, with the results presented in the following Sections 3.1 and 3.2, respectively.

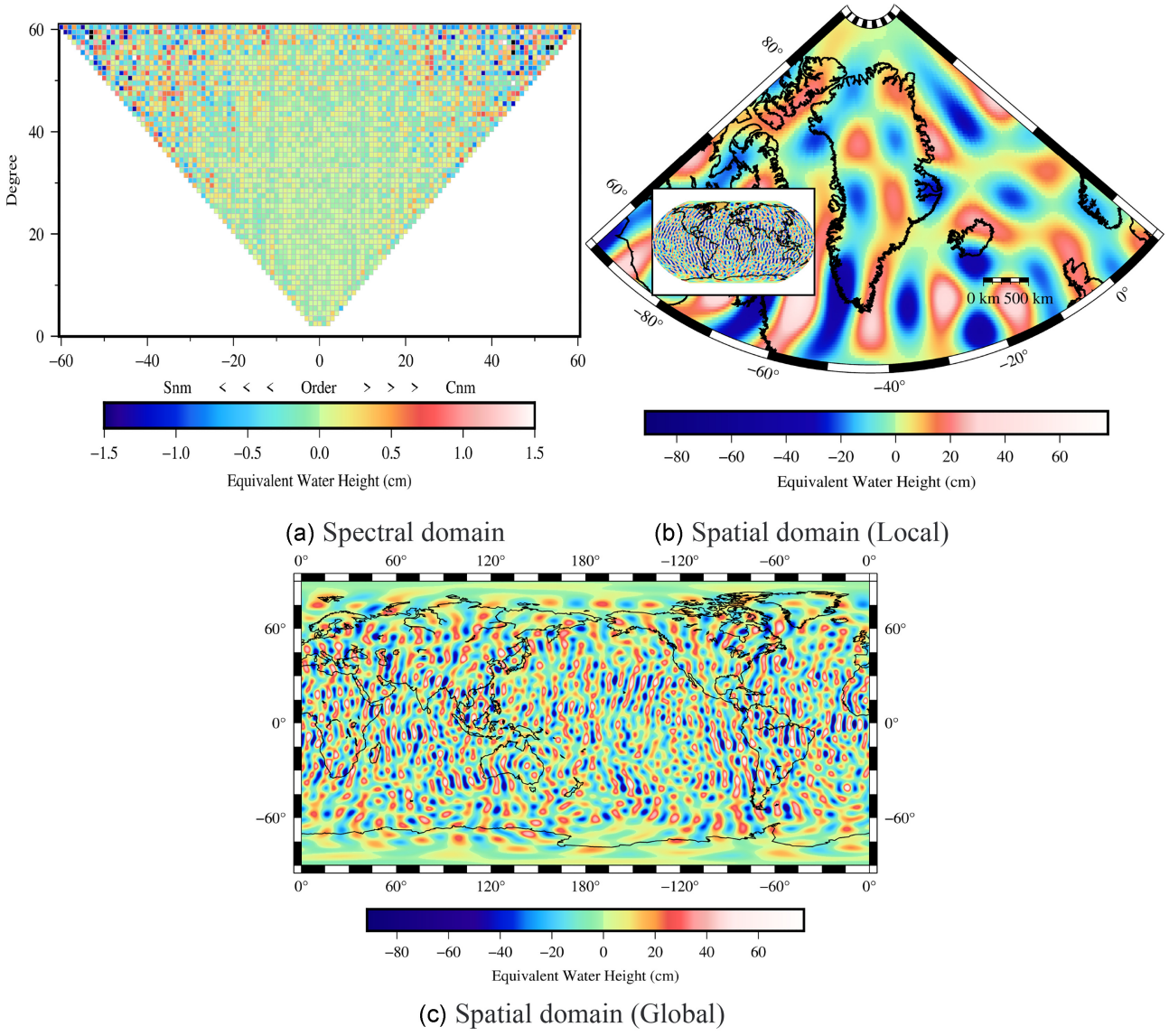

Figure 2. The simulated noise of the SH coefficients. The noise is then added to the SH coefficients of true signals c_{lm} to generate measurements for IA and DA. Degree-0 and degree-1 terms are not considered.

Table 1. The configuration of experimental schemes to be compared: DA and three IAs.

Approaches	Observables	No. of measurements	Distribution of measurements
DA	SH coefficients	3717	—
IA1	potentials	2000	randomly, locally
IA2	potentials	3717	randomly, locally
IA3	potentials	3717	randomly, globally

3.1 Simulation

The Greenland with a buffer zone of about 100 km is chosen as the target area. Similar to Baur & Sneeuw (2011), we first artificially define some mass loss signals around the southeast coast through the following steps: a total of 5000 random values with standard derivation 20 cm are first generated; all the positive values are turned into negative ones by adding a minus sign to simulate the mass loss in terms of equivalent water height (the originally negative values keep unchanged); the mass anomaly values are then arranged in descending order from the southeast coast to the northeast coast. Mass variations other than the target area are assumed all zeros. We do SH analysis with these 5000 samples and the zeros elsewhere and truncated at $l_{max} = 60$, with the SH coefficients denoted as c'_{lm}. These truncated SH coefficients are treated as truth in the spectral domain. Note that for simplicity and without loss of generality, we do not consider the degree-0 and degree-1 terms here. Then the truth in the spatial domain, i.e. the true surface mass variation at any point, can be synthesized according to eq. (18). In

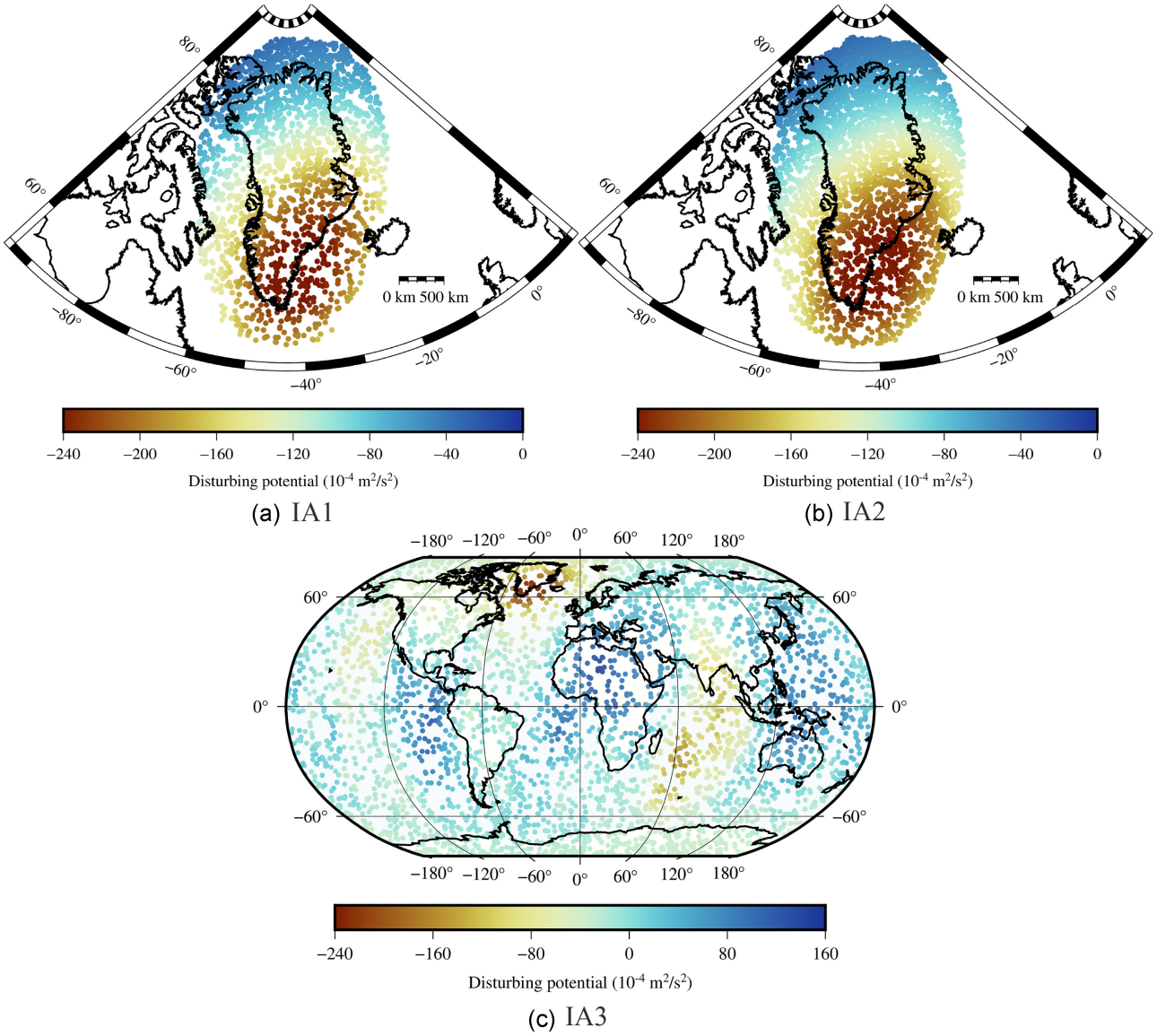

Figure 3. The distributions of pseudo measurements (i.e. disturbing potentials) at 500 km satellite altitude in the three IA approaches. (a) IA1: 2000 measurements distribute locally; (b) IA2: 3717 measurements distribute locally; (c) IA3: 3717 measurements distribute globally. Note the anomalous signals out of the Greenland in Fig. 3(c) result from the added noise.

Fig. 1, we show the truths both in spectral and spatial domains.

$$m(\tilde{\boldsymbol{x}}_i) = \sum_{l=2}^{60} \sum_{m=-l}^{l} c'_{lm} Y_{lm}(\tilde{\boldsymbol{x}}_i) \tag{18}$$

The true SH coefficients of the gravity potential are calculated as $c_{lm} = \frac{3\rho_w}{\rho_E} \frac{1+k_l}{2l+1} c'_{lm}$, where k_l denotes the loading Love number, ρ_w denotes the water density 1000 kg m^{-3} and ρ_E represents the averaged Earth density 5517 kg m^{-3} (Qian *et al.* 2022). The noise of the true SH coefficients $c_{\rm lm}$ are generated using the covariance matrix of CSR GRACE RL05 product in January 2008, denoted as $\Delta_{\rm lm}$ (Baur & Sneeuw 2011). So the input SH coefficients are simulated as $\tilde{c}_{lm} = c_{lm} + \Delta_{lm}$. Fig. 2 shows the simulated noise in both spectral and spatial domains.

We treat the disturbing gravity potentials at 500 km height as pseudo measurements for IA. Three different IA schemes, IA1, IA2 and IA3, with different distributions of pseudo measurements, are considered in this study, as shown in Table 1. In this table, 3717 is the total number of SH coefficients of $l_{\rm max} = 60$, with degree-0 and degree-1 terms excluded. We compare IA1 and IA2 to check if additional pseudo measurements (2000 versus 3717) can provide new information for estimating point-masses and compare IA2 with IA3 to evaluate whether the local or global distribution of pseudo measurements influences the final estimates. In addition, we compare DA with IA1, IA2 and IA3 to test their difference and relationship. The three different pseudo measurement datasets in IA1, IA2 and IA3 are shown in Fig. 3.

As mentioned in Section 2.3, the theoretical proof of the equivalence between DA and IA depends on eq. (13). So it is necessary to evaluate this equivalence numerically, namely to check the difference of the design matrix $\boldsymbol{B}$ in IA from the transformed design matrix $\boldsymbol{FA}$ in

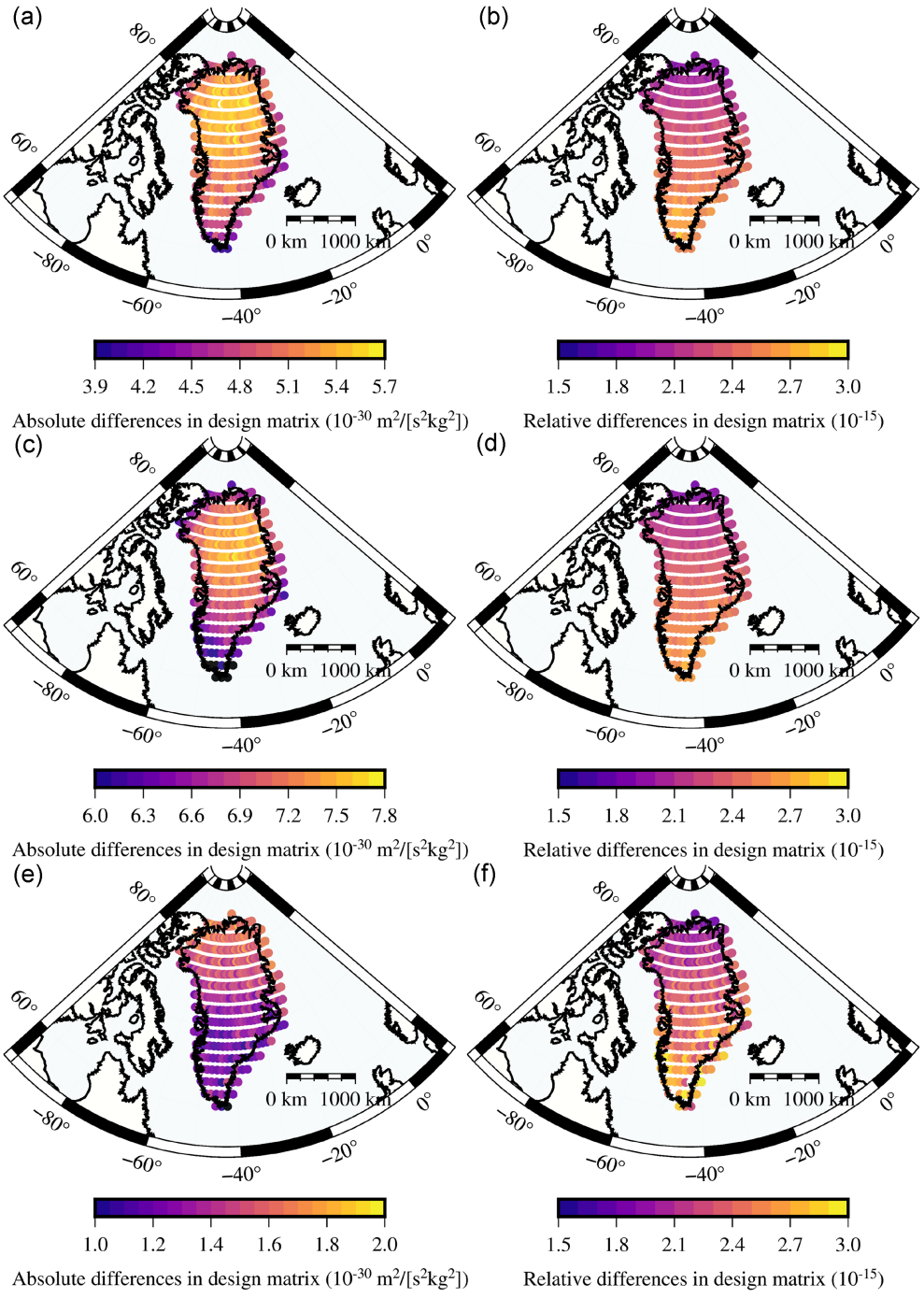

Figure 4. The absolute (left-hand panel) and relative (right-hand panel) difference distribution between the DA and three IAs in the level of design matrices: $\boldsymbol{B}$ in three IAs versus $\boldsymbol{FA}$ in DA. Top: DA versus IA1; Middle: DA versus IA2; Bottom: DA versus IA3. The absolute difference of a point-mass is defined as the L_2-norm of the difference of the corresponding column in $\boldsymbol{B}$ and $\boldsymbol{FA}$. The relative difference of a point-mass is defined as the corresponding absolute difference divided by the L_2-norm of the corresponding column of matrix $\boldsymbol{B}$.

DA. Let the difference between the two sides of eq. (13) be denoted as $[\,\mathbf{c}_1\ \cdots\ \mathbf{c}_{m+l}\,] = \mathbf{C} = \mathbf{B} - \mathbf{FA}$, with $\boldsymbol{c}_i$ being the column vector of $\boldsymbol{C}$, corresponding to the i-th point-mass. Let $\eta_i = \|\mathbf{c}_i\|_2$ and $\bar{\eta}_i = \|\mathbf{c}_i\|_2 / \|\mathbf{b}_i\|_2$ (with $\boldsymbol{b}_i$ being the column vector of $\boldsymbol{B}$) be the absolute and relative differences of i-th point-mass between $\boldsymbol{B}$ and $\boldsymbol{FA}$. The distributions of these differences between DA and three IAs are shown in Fig. 4. It is observed both the absolute and relative differences are at very low numerical levels. We mainly attribute such small differences to the numerical round-off errors, explained as follows: in eqs (1), (3) and (7), the calculation of normalized associated Legendre function involved in Y_{lm} is numerical. In the IA, the pseudo measurements derived from level-2 products in eq. involve such numerical calculation once. The design matrix of IA in eq. (3) involves such numerical calculations twice. As a comparison, in the DA, the measurements (SH coefficients) do not involve such a numerical calculation. The design matrix of DA only involves such numerical calculation once. Considering these

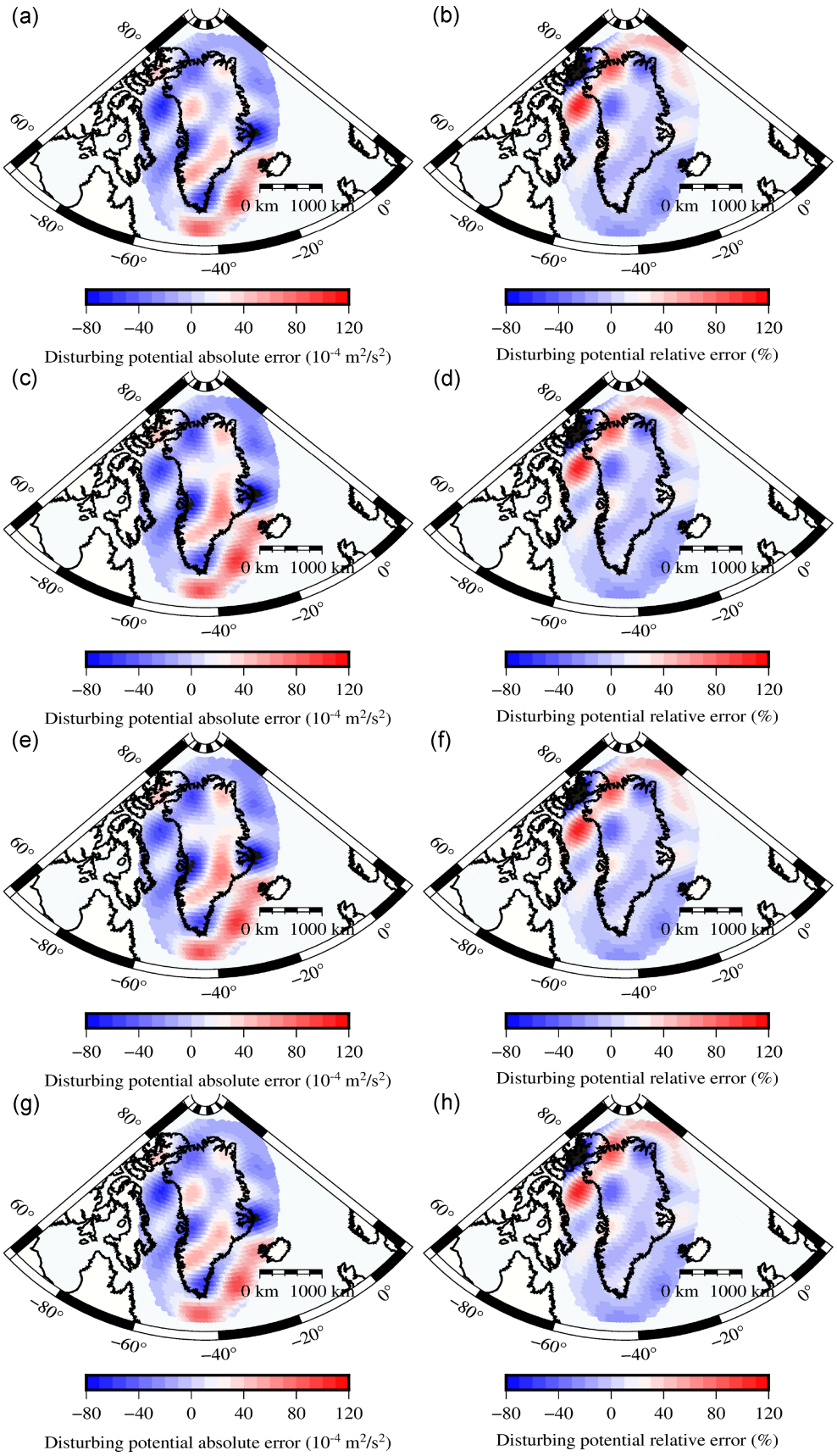

Figure 5. The absolute (the left-hand panel) and relative (the right-hand panel) errors of the 3076 sampled gravity potentials at 5 km altitude of the point-masses estimated from DA (the first row), IA1 (the second row), IA2 (the third row) and IA3 (the last row). The truth of sampled gravity potentials is produced by the true mass anomalies presented in Fig. 1.

Table 2. The error statistics of the gravity potentials for DA and three IAs (unit: 10^{-4} $m^2\,s^{-2}$). The potential errors are calculated as the differences of potentials at a 5-km altitude produced by estimated point-masses and true mass variations.

	Maximum		Minimum		Mean		RMS	STD
Approaches	Absolute	Relative	Absolute	Relative	Absolute	Relative	Absolute	Absolute
DA	99.41	118.9 per cent	−86.76	−123.7 per cent	−1.40	7.1 per cent	29.35	29.32
IA1	104.48	116.3 per cent	−95.64	−136.4 per cent	−0.76	7.6 per cent	33.59	33.58
IA2	104.16	117.0 per cent	−94.45	−139.5 per cent	−0.72	7.2 per cent	33.58	33.57
IA3	99.50	118.9 per cent	−86.03	−122.9 per cent	−1.52	7.3 per cent	29.37	29.33

Table 3. The estimated (simulated) total mass anomalies of the entire Greenland from DA and three IAs (Unit: Gt).

	DA	IA1	IA2	IA3
Total mass anomaly	−309.25	−308.12	−308.11	−309.40

calculations are performed on MATLAB R2018b, whose numerical calculation accuracy is 16 significant digits, it is natural that the relative difference in Fig. 4 is at the level of 10^{-15}. Note this level of difference is the comprehensive impact of many (2000 or 3717) elements in a column of $\boldsymbol{B}$ and $\boldsymbol{FA}$. From this viewpoint, it is round-off errors that causes the differences between DA and IA. Since the relative difference is rather small, it can be neglected. We suppose this proves that eq. (13) indeed holds.

For both IA1 and IA2, the covariance matrix $\boldsymbol{P}$ involved in eq. (5) is singular. We replace the matrix inversion with pseudo inversion (Ran *et al.* 2018b; Klees *et al.* 2019). A total of 376 point-masses, distributed on a $0.5^\circ \times 0.5^\circ$ equiangular grid covering all of Greenland, are to be estimated. For simplicity and without loss of generality, leakage error correction, e.g. by including auxiliary point-masses, is not considered here. The term $g(\boldsymbol{\beta})$ in eq. (5) and eq. (10) is chosen as a Tikhonov regularization term, with an identity regularization matrix (Baur & Sneeuw 2011) and the regularization parameter is optimized using variance component estimation (VCE) approach (Koch & Kusche 2002). Specifically, the chosen regularization parameter is 1.14×10^{-26}.

Considering the true mass variations, denoted in eq. (18), are continuously distributed on the Earth, there are no such things as the true point-masses. So we cannot directly assess the inversion error for a specific point-mass estimate. Instead, an indirect assessment is performed here. We compare the disturbing gravity potentials at 5-km height generated by the estimated point-masses with that generated by the true mass variations c_{lm}. The absolute and relative (with respect to truth) gravity potential errors are shown in Fig. 5, respectively, with the error statistics presented in Table 2. The error distributions of the four approaches are almost the same patterns. From Table 2, all approaches have a systematic bias of ∼7 per cent and we attribute it to the added noise. In general, the four approaches perform comparably, with the DA and the global IA3 being slightly superior to the other two. In our understanding, the measurements in DA, namely the SH coefficients, correspond to the globe. These measurements code the information on the entire reference ellipsoid. In IA3, the pseudo measurements are just randomly globally distributed. Therefore, there is a better agreement between DA and IA3. To summarize, in terms of the gravity potential error, the DA and IA can be viewed as being practically equivalent to each other.

The total mass variations across Greenland estimated from the four approaches are shown in Table 3. The differences among the four approaches are small, with the biggest difference between the DA and IAs being 1.14 Gt (between DA and IA2). The estimated point-masses of DA and three IAs and their absolute and relative differences, defined in eq. (19), are shown in Fig. 6. In general, all the DA and IAs produce the very similar estimates and DA and IA3 behave more closer than others, which is consistent with the results in Table 2. The maximum absolute differences of each point-mass are approximately within 1 Gt. The large relative differences are mainly due to the small signal values over there (comparing the left-hand panel with the right-hand panel in Fig. 6). In terms of the estimated point-masses, the DA and the IA can be viewed as being practically equivalent to each other.

$$\begin{cases} \xi_i^{(\mathrm{abs.})} = \hat{\beta}_i^{(\mathrm{DA})}(k) - \hat{\beta}_i^{(\mathrm{IA})}(k) \\ \xi_i^{(\mathrm{rel.})} = \dfrac{\hat{\beta}_i^{(\mathrm{DA})}(k) - \hat{\beta}_i^{(\mathrm{IA})}(k)}{\hat{\beta}_i^{(\mathrm{DA})}(k)} \end{cases} \tag{19}$$

3.2 Real GRACE data analysis

The real data processed here is the monthly CSR GRACE RL05 SH coefficient solutions, with their full covariance matrices, ranging from January 2003 to December 2012. The maximum SH degree is 60. The data in the following months are absent: June 2003, January 2011, June 2011, May 2012 and October 2012. The following preprocessing steps are performed first for the monthly SH solutions. First, the degree-1 coefficients are added (Sun *et al.* 2016) and the C_{20} coefficients derived by Satellite Laser Ranging are replaced (Loomis *et al.* 2020). Secondly, a glacial isostatic adjustment (GIA) correction is applied based on the ICE6G-D model (Peltier *et al.* 2018). Finally, the 2004.000–2009.999 mean baseline is removed. The residual SH coefficients are then directly treated as measurements in DA and transformed into pseudo measurements (disturbing potentials) in IAs.

Taking the estimated point-masses in April 2004 as examples, Fig. 7 shows the estimates and their absolute and relative differences between DA and three IAs, as defined in eq. (19). It is observed that most of the absolute differences are within 1 Gt. We also find the

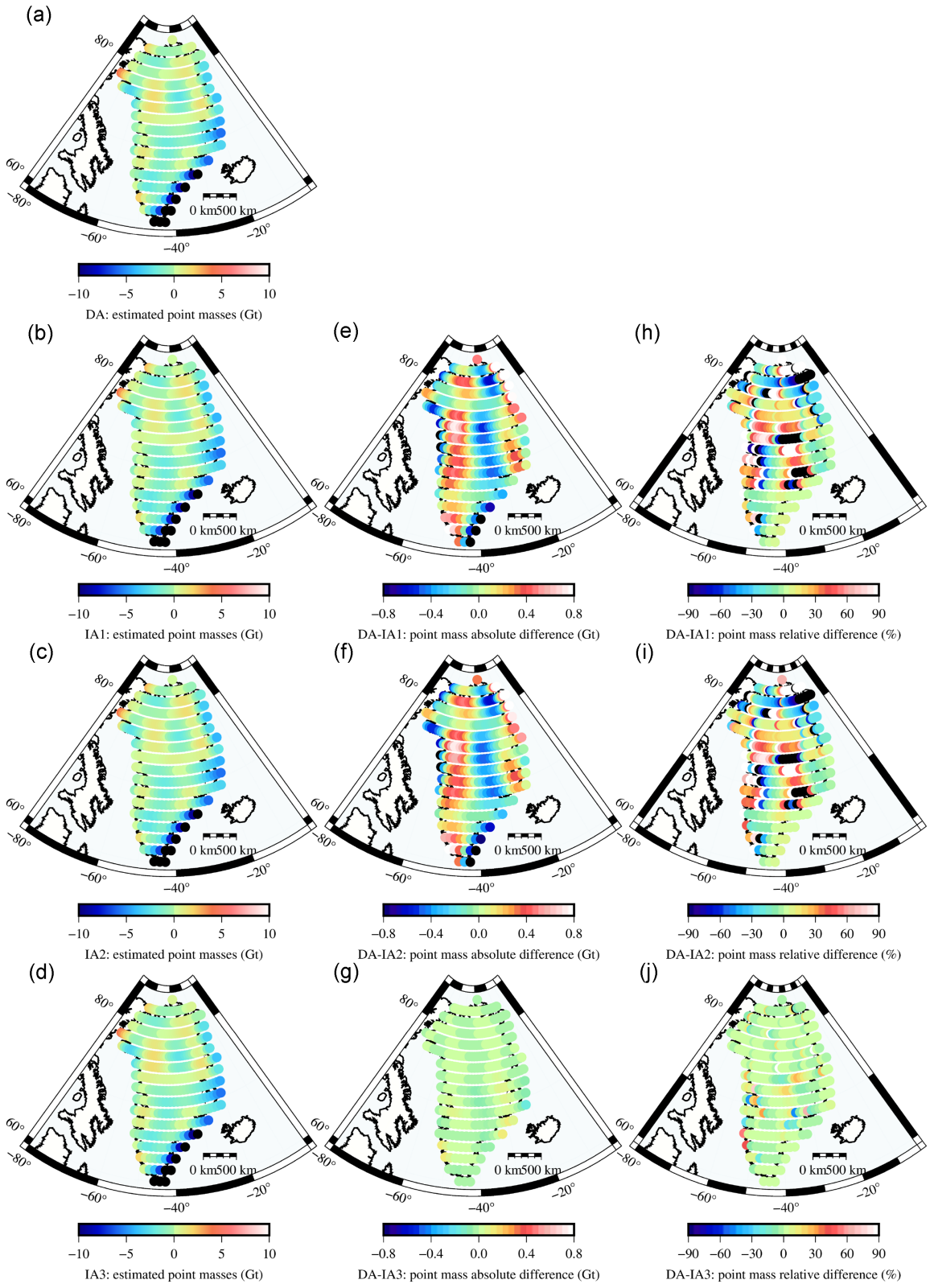

Figure 6. The estimated simulated point-masses (the left-hand panel) and their absolute (the middle panel) and the relative (the right-hand panel) differences between DA and IA1 (the second row), IA2 (the third row), IA3 (the last row). The extremely large relative differences in Figs. (h) and (i) are due to the weak signals there as shown in Figs. (b) and (c).

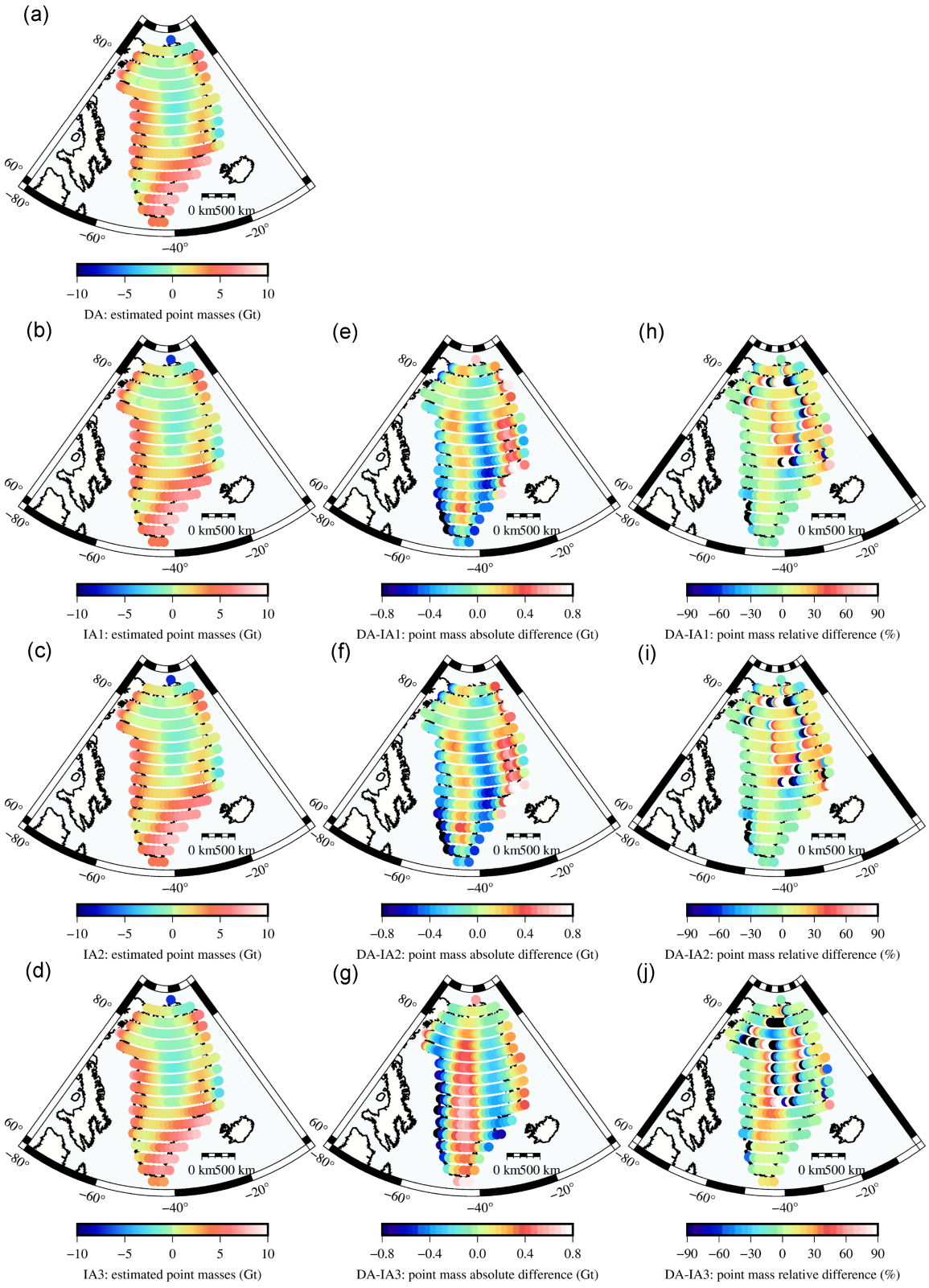

Figure 7. The estimated point-masses (the left-hand panel) and their absolute (the middle panel) and the relative (the right-hand panel) differences between DA and IA1 (the second line), IA2 (the third line), IA3 (the last line) in April 2004. The extremely large relative differences in (h), (i) and (j) are due to the weak signals there as shown in (b), (c) and (d).

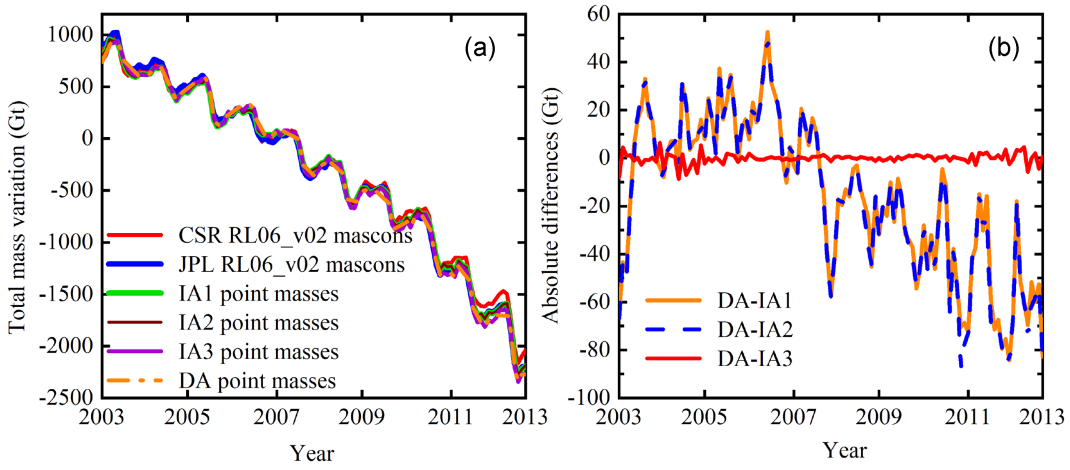

Figure 8. Time series of the total mass anomaly in Greenland from January 2003 to December 2012. (a): the estimated DA and three IAs point-mass solutions and the CSR RL06_v02 mascon and JPL RL06_v02 mascon solutions; (b): the absolute differences of the total mass anomaly between DA and three IAs. All the mass anomalies are respect to the 2004.000–2009.999 time mean baseline.

differences correlated with the magnitude of the mass signal. There are large absolute differences (∼1 Gt) on the southeast and west coast of Greenland. However, the relative difference is small there. In central Greenland, the opposite is true. This is due to significant mass loss along the southeast and west of Greenland, while there is no significant mass variation in central Greenland (Ran *et al.* 2018b).

The point-mass estimates of both DA and IAs are compared with the latest CSR RL06_v02 (Save *et al.* 2016) and the JPL RL06_v02 mascon products (Watkins *et al.* 2015). Note that both the released mascons and our estimated point-mass solutions use the same GIA correction, namely ICE-6G_D model (Peltier *et al.* 2018). Fig. 8(a) presents the time series of the estimated total mass anomaly across Greenland of DA and three IAs, with those of CSR and JPL mascons for comparisons. The seasonal variation of these time series is consistent. We also notice some deviations (especially after 2011) between CSR RL06_v02 solution and IA, DA solutions. However, considering both IA and DA point-mass solutions agree well with JPL RL06_v02 mascon solutions, investigating the causes of the differences between the in-house point-mass solutions and CSR mascon solutions is beyond the scope of this study. Fig. 8(b) shows the absolute differences of total mass anomalies between DA and three IAs. The proposed DA again perform closer to IA3 as we found before. To conclude, the proposed DA produces the comparable mass anomaly estimates as the other released mascons solutions, which again demonstrates the feasibility of directly using GRACE level-2 SH coefficients as measurements for calculating surface mass variations.

4 CONCLUDING REMARKS

In this study, we have shown how to carry out a statistically optimal point-mass inversion by directly using GRACE level-2 SH coefficients as measurements. The statistical optimality is in the sense of appropriately weighing the measurements according to the data covariance matrix. The validity of this direct approach and its equivalence to the conventional indirect approaches were both theoretically proven and experimentally demonstrated through simulation and real data processing. Choosing and calculating pseudo measurements, propagating covariance matrix and (potentially) dealing with the singularity of covariance matrix involved in indirect approaches can be avoided in the direct approach.

The statistically optimal direct approach can be readily employed in mascon inversion of the GRACE data and other radial basis functions-based approaches in regional gravity modeling. The performance of this approach in these applications will be investigated in future studies.

ACKNOWLEDGMENTS

Prof Jurgen Kusche and Prof Jingxiang Gao are highly acknowledged for their help in linguistics during the preparation of this manuscript. The support provided by the China Scholarship Council (CSC) during Nijia's visiting to Delft University of Technology is also acknowledged. Gratitude is also extended to Wei Feng for providing the GRACE MATLAB Toolbox (GRAMAT) (Feng 2019), CSR for providing GRACE RL06 level-2 products and RL06_v02 mascons and JPL for RL06_v02 mascons. This work is sponsored partially by the National Natural Science Foundation of China (Grant Number: 42074001 and 41974026), partially by the State Key Laboratory of Geo-Information Engineering (Grant Number: SKLGIE2020-Z-1–1), partially by the Postgraduate Research & Practice Innovation Program of Jiangsu Province (Grant Number: KYCX21_2292) and partially by the Postgraduate Innovation Program of China University of Mining and Technology (Grant Number: 2021WLKXJ098).

DATA AVAILABILITY

The CSR GRACE RL05 products with both SH coefficients and their covariance matrices are downloaded at http://download.csr.utexas.edu/outgoing/grace/; The CSR GRACE RL06_v02 mascon products are download at https://www2.csr.utexas.edu/grace/RL06_mascons.html; The JPL GRACE RL06_v02 mascons are download at https://grace.jpl.nasa.gov/data/get-data/jpl_global_mascons/.

REFERENCES

Barletta, V.R., Sørensen, L.S. & Forsberg, R., 2013. Scatter of mass changes estimates at basin scale for Greenland and Antarctica. *Cryosphere,* **7,** 1411–1432.

Baur, O. & Sneeuw, N., 2011. Assessing Greenland ice mass loss by means of point-mass modeling: a viable methodology. *J. Geod.,* **85,** 607–615.

Croteau, M.J., Nerem, R.S., Loomis, B.D. & Sabaka, T.J., 2020. Development of a Daily GRACE Mascon Solution for Terrestrial Water Storage. *J. Geophys. Res.: Solid Earth,* **125,** e2019JB018468, doi:10.1029/2019JB018468.

Feng, W., 2019. GRAMAT: a comprehensive Matlab toolbox for estimating global mass variations from GRACE satellite data. *Earth Sci. Inf.,* **12,** 389–404.

Ferreira, V.G., Yong, B., Seitz, K., Heck, B. & Grombein, T., 2020a. Introducing an Improved GRACE Global Point-Mass Solution—A Case Study in Antarctica. *Remote Sensing,* **12,** 3197, doi:10.3390/rs12193197.

Ferreira, V.G., Yong, B., Tourian, M.J., Ndehedehe, C.E., Shen, Z., Seitz, K. & Dannouf, R., 2020b. Characterization of the hydro-geological regime of Yangtze River basin using remotely-sensed and modeled products. *Sci. Total Environ.,* **718,** 137354, doi:10.1016/j.scitotenv.2020.137354.

Forsberg, R., Sorensen, L. & Simonsen, S., 2017. Greenland and Antarctica ice sheet mass changes and effects on global sea level. *Surv. Geophys.,* **38,** 89–104.

Jacob, T., Wahr, J., Pfeffer, W.T. & Swenson, S.C., 2012. Recent contributions of glaciers and ice caps to sea level rise. *Nature,* **482,** 514–518.

Klees, R., Revtova, E., Gunter, B.C., Ditmar, P., Oudman, E., Winsemius, H.C. & Savenije, H.H.G., 2008. The design of an optimal filter for monthly GRACE gravity models. *Geophys. J. Int.,* **175,** 417–432.

Klees, R., Slobbe, D.C. & Farahani, H.H., 2018. A methodology for least-squares local quasi-geoid modelling using a noisy satellite-only gravity field model. *J. Geod.,* **92,** 431–442.

Klees, R., Slobbe, D.C. & Farahani, H.H., 2019. How to deal with the high condition number of the noise covariance matrix of gravity field functionals synthesised from a satellite-only global gravity field model? *J. Geod.,* **93,** 29–44.

Koch, K.R. & Kusche, J., 2002. Regularization of geopotential determination from satellite data by variance components. *J. Geod.,* **76,** 259–268.

Loomis, B.D., Rachlin, K.E., Wiese, D.N., Landerer, F.W. & Luthcke, S.B., 2020. Replacing GRACE/GRACE-FO C-30 With Satellite Laser Ranging: impacts on Antarctic Ice Sheet Mass Change. *Geophys. Res. Lett.,* **47,** doi:10.1029/2019GL085488.

Peltier, W.R., Argus, D.F. & Drummond, R., 2018. Comment on "An Assessment of the ICE-6G_C (VM5a) Glacial Isostatic Adjustment Model" by Purcell et al. *J. Geophys. Res.-Solid Earth,* **123,** 2019–2028.

Qian, N., Chang, G., Ditmar, P., Gao, J. & Wei, Z., 2022. Sparse DDK: a Data-Driven Decorrelation Filter for GRACE Level-2 Products. *Remote Sensing,* **14,** 2810, doi:10.3390/rs14122810.

Ran, J., Ditmar, P., Klees, R. & Farahani, H.H., 2018a. Statistically optimal estimation of Greenland Ice Sheet mass variations from GRACE monthly solutions using an improved mascon approach. *J. Geod.,* **92,** 299–319.

Ran, J., Ditmar, P. & Klees, R., 2018b. Optimal mascon geometry in estimating mass anomalies within Greenland from GRACE. *Geophys. J. Int.,* **214,** 2133–2150.

Richter, A., Groh, A., Horwath, M., Ivins, E.R., Marderwald, E., Hormaechea, J.L., Perdomo, R. & Dietrich, R., 2019. The Rapid and Steady Mass Loss of the Patagonian Icefields throughout the GRACE Era: 2002–2017. *Remote Sensing,* **11,** 909, doi:10.3390/rs11080909.

Save, H., Bettadpur, S. & Tapley, B.D., 2016. High-resolution CSR GRACE RL05 mascons. *J. Geophys. Res.: Solid Earth,* **121,** 7547–7569.

Schmidt, M., Fengler, M.J., Mayer-Gürr, T., Eicker, A., Kusche, J., Sanchez, L. & Han, S., 2007. Regional gravity modeling in terms of spherical base functions. *J. Geod.,* **81,** 17–38.

Schrama, E.J.O. & Wouters, B., 2011. Revisiting Greenland ice sheet mass loss observed by GRACE. *J. Geophys. Res.: Solid Earth,* **116,** B02407, doi:10.1029/2009JB006847.

Slobbe, C., Klees, R., Farahani, H.H., Huisman, L., Alberts, B., Voet, P. & De Doncker, F., 2019. The Impact of Noise in a GRACE/GOCE Global Gravity Model on a Local Quasi-Geoid. *J. geophys. Res.,* **124,** 3219–3237.

Sørensen, L.S., Jarosch, A.H., Aðalgeirsdóttir, G., Barletta, V.R., Forsberg, R., Pálsson, F., Björnsson, H. & Johannesson, T., 2017. The effect of signal leakage and glacial isostatic rebound on GRACE-derived ice mass changes in Iceland. *Geophys. J. Int.,* **209,** 226–233.

Su, Y., Zheng, W., Yu, B., You, W., Yu, B. & Xiao, D., 2019. Surface mass distribution derived from three-dimensional acceleration point-mass modeling approach with spatial constraint methods. *Chinese J. Geophys.,* **62,** 508–519.

Sun, Y., Riva, R. & Ditmar, P., 2016. Optimizing estimates of annual variations and trends in geocenter motion and J(2) from a combination of GRACE data and geophysical models. *J. Geophys. Res.-Solid Earth,* **121,** 8352–8370.

Tapley, B.D. *et al.*, 2019. Contributions of GRACE to understanding climate change. *Nature Climate Change,* **9,** 358–369.

Wahr, J., Molenaar, M. & Bryan, F.O., 1998. Time variability of the Earth's gravity field : hydrological and oceanic effects and their possible detection using GRACE. *J. geophys. Res.,* **103,** 30205–30229.

Watkins, M.M., Wiese, D.N., Yuan, D.- N., Boening, C. & Landerer, F.W., 2015. Improved methods for observing Earth's time variable mass distribution with GRACE using spherical cap mascons. *J. Geophys. Res.-Solid Earth,* **120,** 2648–2671.

Wittwer, T., 2009. *Regional Gravity Field Modelling with Radial Basis Functions*. Delft University of Technology, Delft, The Netherlands.

Wouters, B., Bonin, J.A., Chambers, D.P., Riva, R.E., Sasgen, I. & Wahr, J., 2014. GRACE, time-varying gravity, Earth system dynamics and climate change. *Rep. Prog. Phys.,* **77,** 116801, doi:10.1088/0034-4885/77/11/116801.

Yi, S. & Sun, W., 2014. Evaluation of glacier changes in high-mountain Asia based on 10 year GRACE RL05 models. *J. Geophys. Res.: Solid Earth,* **119,** 2504–2517.